Strain Rate Estimation from Ultrasound Channel Data

Vincent van de Schaft and Ruud J. G. van Sloun

Eindhoven University of Technology, Eindhoven, The Netherlands
{v.v.d.schaft,r.j.g.v.sloun}@tue.nl

Abstract. Ultrasound Strain rate estimation provides a quantitative measure of cardiac muscle function, which makes it an important tool for the diagnosis and monitoring of heart disease. The most common approach for strain rate estimation, speckle tracking through block matching, assumes the matching block undergoes a rigid translation between frames, which is not true in strained tissue. We present a method for estimating the strain rate by tracking off-grid point scatterers between transmissions in the channel data. Our method attempts to reconstruct the observed signals as a sum of point sources, akin to Gaussian Splatting. We evaluate our method on 2D simulated phantom data and show we obtain lower error in the estimated strain rate maps and are better able to detect an ischemic region in the myocardium. We also show that our method is able to recover strain rate maps from in-vivo data. All code is available at `https://github.com/vincentvdschaft/strain-off-grid`.

Keywords: Motion Tracking · Ultrasound · Model Based.

1 Introduction

Myocardial strain estimation using ultrasound provides a quantitative measure for cardiac muscle function. As such it has become an essential tool for understanding and diagnosing various cardiovascular diseases. It is used to diagnose ischemic heart disease[17], where pathological tissue in the myocardium is characterized by reduced strain. Strain imaging also plays a role in monitoring the treatment of heart disease[3].

Myocardial strain estimation was first developed in the 1990s using the technique of pulsed wave tissue Doppler (TD)[2]. In TD the phase shift between two consecutive transmissions is measured by correlating the beamformed scanlines. This method gives accurate velocity estimates along the direction of the ultrasound beam, but does not provide lateral motion estimation. More recently various image based methods have become popular and have been proven in the clinic[6]. The most prominent image based technique is speckle tracking[1, 15] through block matching. Block matching, like TD, works by correlating a block of data with a block in a subsequent frame to estimate the motion of the tissue. Because it operates in the image domain, block matching can estimate motion in both the axial and lateral directions.[5, 7]

A core limitation of correlation based tracking methods like block matching based speckle tracking is that they make the assumption that a block of tissue undergoes a rigid translation between two frames. This assumption is necessarily violated in strain rate estimation as the very definition of strain is that the tissue is stretched and compressed. Block matching methods can still obtain strain maps because more distant points can move differently, but are limited by a fundamental trade-off: To get a robust match between frames we want to use a larger matching window, but this will make the assumption of rigid translation less valid. This in turn leads to blurred or inaccurate strain maps.

In this work we present a method for estimating the strain rate by estimating 2D tissue motion vectors from the raw channel data. Our approach is fundamentally different from existing methods in that it does not obtain motion vectors by using correlation, like block matching speckle tracking or TD methods. Instead we define a physical model for the acquisition process and track simulated point scatterers between transmissions to reproduce the observed data. In this sense our approach is similar to the concept of Gaussian Splatting[8], with ultrasonic backscatter responses instead of Gaussians. The approach is also similar to existing work on model-based ultrasound imaging, but has not been applied to strain rate estimation[16]. Our approach allows for the estimation of local strain rates from closely spaced points.

2 Methods

We fit a set of point scatterers to the measured channel data. Each point scatterer has a position in every transmission, forming a trajectory through space. The idea is to fit these tracks such that they reproduce the measured channel data. We initialize points in a track in the same location. This way we can assume that the points after fitting actually represent the motion of a single point in the tissue (given that the tissue motion between transmissions is not too large). The displacements of the points in these tracks are then used to compute the strain rate map.Fig. 1 shows a simplified overview of the proposed method.

2.1 Notation

Vectors are denoted by boldfaced characters and tensors are denoted by capital characters. We will denote an element of a vector $\mathbf{x}$ by $x[i]$. An element of a tensor X will be denoted by $X[i, j, k]$ where i, j, k are the indices along each dimension. We will denote the Real Fourier Transform (RFT) of a signal $x(t)$ by $\widetilde{x}(f)$. Quantities that that are adapted during the optimization process will be denoted by the variable with an underline, e.g. $\underline{x}$.

2.2 Acquisition model

We begin by describing the ultrasound system. When acquiring a frame, the ultrasound system has N_{CH} channels, which are connected to the same number

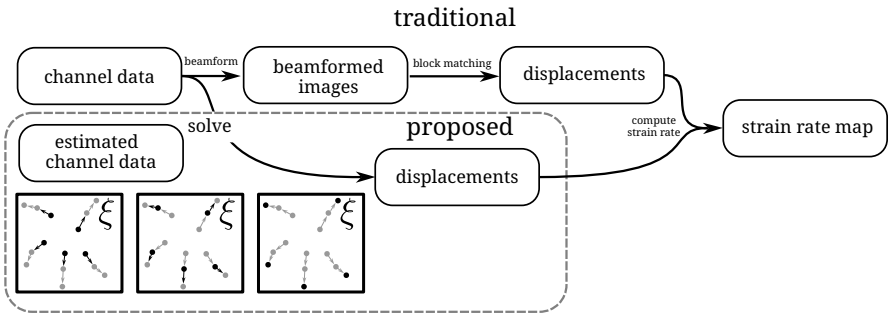

Fig. 1. Overview of the proposed method versus the traditional block matching method. The displacements are estimated by fitting trajectories to reproduce the measured channel data over 3 frames.

of transducer elements. To acquire a frame, the ultrasound system performs N_{TX} transmissions (e.g. it emits N_{TX} plane waves). For every transmission it records N_{AX} samples per channel.

In this way, the system captures a tensor of radio frequency (RF) data $Y \in \mathbb{R}^{N_{\mathrm{TX}} \times N_{\mathrm{AX}} \times N_{\mathrm{CH}}}$. We apply the RFT to the RF data Y to obtain $\widetilde{Y} \in \mathbb{C}^{N_{\mathrm{TX}} \times N_{\mathrm{FB}} \times N_{\mathrm{CH}}}$, where N_{FB} is the number of frequency bins. We denote a single element of $\widetilde{Y}$ by $\widetilde{y}_n$.

This element $\widetilde{y}_n$ has a corresponding transmission index tx_n, frequency bin index fb_n and channel index ch_n. The frequency corresponding to frequency bin fb_n is denoted by fn, with corresponding angular frequency ωn. The center frequency of the transmitted pulse is denoted by f_c. The sampling rate of the system is denoted by f_s.

Forward model We pose the problem of tissue tracking as an inverse problem. We define a differentiable forward model h that computes an estimate of the RF data $\widetilde{Y}^*$ from a collection of point scatterers. As such, the forward model h is an ultrasound channel data simulator. This simulator takes a set of input variables ξ including the locations of all scatterers. With this input the simulator produces an output sample $\widetilde{y}_n^*$:

$$\widetilde{y}_n^* = h(\xi, n). \tag{1}$$

The problem we seek to solve is then to find the input variables ξ that reproduce the measured RF data $\widetilde{Y}^*$.

In order to solve this inverse problem, we consider chunks of N'_{TX} frames, where N'_{TX} can be as low as 2 or as high as 5 or 7. In the results presented here we always use $N'_{\mathrm{TX}} = 3$. We model the target scatterers as a collection of N_{PTS} point sources. These point sources have a location in every transmission $P_s \in \mathbb{R}^{N_{\mathrm{PTS}} \times N'_{\mathrm{TX}} \times 2}$ and an intensity in every frame $\underline{\mathbf{m}} \in \mathbb{R}^{N_{\mathrm{PTS}} \times N'_{\mathrm{TX}}}$. Thus, $\xi = \{P_s, \underline{\mathbf{m}}\}$.

From this we compute the channel data sample $\widetilde{y}_n^*$ as the sum of the responses of all scatterers

$$\widetilde{y}_n^* = \sum_{i=0}^{N_{\text{PTS}}-1} \Bigg[\overbrace{\widetilde{\eta}\left(\omega\left[n\right]\right)}^{\text{waveform}} \cdot \overbrace{b\left(\theta_{\text{rx}}\left[i,n\right], fn\right)}^{\text{directivity}} \cdot \overbrace{\widetilde{q}\left[n\right]}^{\text{TGC}} \cdot \overbrace{\mu\left[n\right]}^{\text{attenuation}} \cdot \overbrace{\exp\left(-j\omega\left[n\right]\tau_{\text{total}}\right)}^{\text{delay}} \cdot \overbrace{\frac{10^{-4}}{\tau_{\text{tx}}\tau_{\text{rx}}c}}^{\text{spread}} \cdot \overbrace{\underline{m}\left[i,\text{tx}_n\right]}^{\text{magnitude}} \Bigg]. \tag{2}$$

Here $b(\theta_n, fn)$ is the angle dependent directivity of the transducer elements [13], which is given by:

$$b\left(\theta, f\right) = \text{sinc}\left(w\frac{c}{f}\sin\left(\theta\right)\right)\cos\left(\theta\right) \tag{3}$$

For the transmit waveform we use a Gaussian-windowed sinusoid of unit amplitude.

$$\widetilde{\eta}(f) = -j\sigma\sqrt{2\pi}\exp\left(-2\left(\omega-\omega_c\sigma\right)^2\right). \tag{4}$$

The total delay for sample n from scatterer i, $\tau_{\text{total}}\left[i,n\right]$, is computed as the sum of four components. The transmit delay $\tau_{\text{tx}}\left[i,n\right]$, which is the travel time from transducer to scatterer. The receive delay $\tau_{\text{rx}}\left[i,n\right]$, which is the travel time from scatterer back to the transducer element that records sample n. The time-to-peak τ_{peak} of the transmit pulse. And the transmit delay offset $\tau_0\left[n\right]$, which accounts for the time offset of the individual elements for focusing. The transmit and receive time-of-flights τ_{tx} and τ_{rx} are computed using a simple geometric model of the transducer and medium assuming a constant speed of sound c as $\tau_{\text{total}} = \tau_{\text{tx}} + \tau_{\text{rx}} + \tau_{\text{peak}} + \tau_0$

Optimization We begin by beamforming the channel data of the middle transmit out of the N'_{TX} frames at $\lambda/2$ resolution and detecting peaks in the beamformed data using a simple pixel-wise peak detection algorithm. We initialize $\underline{P_s}$ on the brightest N_{PTS} peaks. We use the zea toolbox for the beamforming [14]. We then initialize $\underline{P_s}$ on these peak locations. We initialize $\underline{\mathbf{m}} \sim \mathcal{N}\left(0, 10^{-4}\right)$. We start by fitting only the middle frame for 6000 iterations, after which we add one frame on each side every 6000 iterations until all N'_{TX} frames are included. When adding the surrounding frames, the positions of the scatterers are initialized at the same location as the earlier/later point in each track. We use the Adam optimizer with a learning rate of 10^{-3}[9].

The loss function we minimize is given by:

$$\mathcal{L}(\xi) = \left\| \sum_{n=0}^{N} \widetilde{y}_n - h(\xi, n) \right\|_2^2 + \lambda \left\|\mathbf{a}\right\|_2^2, \tag{5}$$

where $\mathbf{a}$ is the acceleration of the scatterers over the N'_{TX} transmissions. The regularization on the acceleration encourages straight trajectories for the scatterers as opposed to trajectories that jump around. We set $\lambda = 10^{-3}$ for all experiments.

2.3 Data

Simulated Data We construct two digital phantoms to represent the myocardium. The first is a simple short axis phantom, which resembles the parasternal short-axis view. We set the inner diameter after diastole to 40 mm in order to have a realistic value for both male and female hearts [4]. During the cardiac cycle the phantom contracts, which we model by shrinking both the inner and outer diameter of the ring in such a way that the thickness of the ring increases. We also include a small rotation around the center of the ring, which reaches a maximum of 10°, to model the twisting motion of the heart[11].

The second phantom resembles the apical two-chamber (A2CH) view, which we will refer to as long axis phantom. We use this phantom to simulate a myocardium with an ischemic section to investigate whether it is visible in the computed strain rate map. This phantom was created by manually drawing a sequence of connected boxes on top of a sample from the CAMUS *in-vivo* dataset [10]. We follow the mask in the CAMUS dataset, which was drawn by a physician. We sample scatterers uniformly within the myocardium. We define curves for the variation in length and width of the segments and solve for the locations of the vertices of the boxes at every time step. The scatterers are moved with the boxes by defining their position in the coordinates of their respective box and transforming them to the global coordinates of the phantom. The ischemic section is defined by setting the amplitude of the lengthening of some of the boxes to zero.

We simulated the channel data using the simulator in the open source Zea toolbox[14]. For both phantoms we simulate 10,000 scatterers per frame. Because we are simulating motion between transmissions, we need to determine a realistic pulse repetition frequency (PRF). The reference acquisition used images up to a depth of 150 mm. Given a sound speed of 1540 m/s, this means that the round trip time for one transmission is around 0.2 ms. Since cardiac imaging is typically performed with harmonic imaging, we will assume we need to do two transmissions to apply pulse inversion. This yields a maximum PRF of 2566 Hz. We therefore set the PRF to 2000 Hz as a conservative estimate.

In-vivo Data We also apply our method to some publically available *in-vivo* data that was acquired on a healthy volunteer using a Verasonics Vantage 256 system with Philips S5-1 transducer[18]. The acquisition consists of a harmonic imaging sequence with 10 diverging wave transmissions with a focal depth of -10mm. The acquisition captures an apical four-chamber (A4CH) view.

2.4 Computing Strain Rate Maps

After we have estimated the locations of our scatterers and their corresponding motion vectors, we need to compute the strain rate map from these vectors. We do this by computing a local strain rate matrix for scatterer. For scatterer we find the other scatterers that are within a radius of 5mm. We then fit an affine transformation from the first frame to the last frame. The matrix of this transformation is assigned to the centroid position of the scatterers. After this we have a set of scalar points. To compute a dense strain rate map we apply Gaussian smoothing to the values with a standard deviation of 5mm. We do this by initializing a map of zeros and for every point we add the value of the point multiplied by the gaussian kernel to the map. We then divide this map by a map that is constructed in the same way, but with all points set to 1. This yields a dense strain rate map.

2.5 Experiments

We compare our method to a block matching speckle tracking algorithm. In block matching a window around a point is compared to all windows within a search range in the next frame. The displacement is then estimated as the displacement that maximizes the similarity between the windows[19]. We use normalized cross correlation as the similarity metric. We use a window size of 21x21 and a search range of 42x42 for all experiments. We beamform the channel data using the Zea toolbox[14] using Delay-Multiply-and-sum beamforming [12]. Finally we apply envelope detection and log compress the data to a dynamic range of 60 dB. The resulting images are mapped to the range $[0, 1]$ and used as input to the block matching algorithm.

3 Results

Fig. 2 shows the short axis phantom and the recovered strain rate curves for three reference positions A, B, and C. These reference positions are defined in the first frame and then translated with the known motion of the phantom for the following frames. The figure shows that Channel Data Tracking (CDT) consistently adheres better to the ground truth strain rate curves than block matching. For the estimation of radial strain, both methods struggle, but we find that the block matching algorithm severely overestimates the strain rate compared to CDT.

Fig. 3 shows the long axis phantom and the recovered strain rate maps for a reference position inside the ischemic region and a reference position outside the ischemic region. We see that CDT is able to recover the ischemic region in the myocardium, while block matching produces inaccurate estimations in the ischemic region.

Table 1 shows the average error in the strain rate maps for the two simulated phantoms. We see consistently lower error for CDT. These numbers confirm what we see in Figs. 2 and 3.

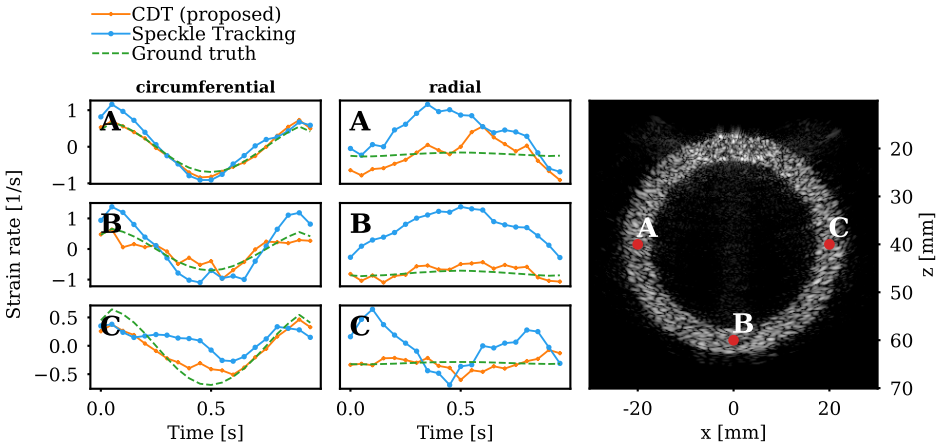

Fig. 2. The short axis phantom and the recovered strain rate curves for three different positions in the phantom.

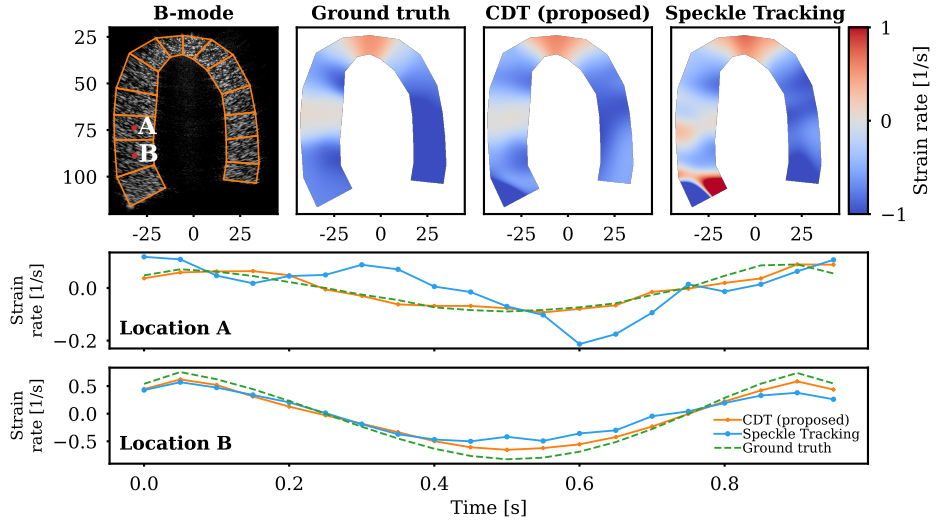

Fig. 3. The long axis phantom and the recovered strain rate maps for points inside and outside the ischemic region.

Fig. 4 shows the recovered longitudinal strain rate maps for the in-vivo dataset of a frame during systole (strain in the z-direction), masked based on beamformed image intensity. The strain is computed along the z-axis. While there is no ground truth available we do see we recover plausible strain rate maps. During systole, we expect negative strain rates as the myocardium contracts. In the septum we find plausible strain rate values in the interval [-2, 2]. We should note here that we have used an *in-vivo* acquisition which does not do repeated transmissions, but uses diverging waves at 5° intervals. This makes the problem more challenging for both methods. To further investigate the performance of our method, it would be necessary to acquire a dataset with repeated diverging wave transmissions, which would allow for a more robust estimation of the strain rate maps.

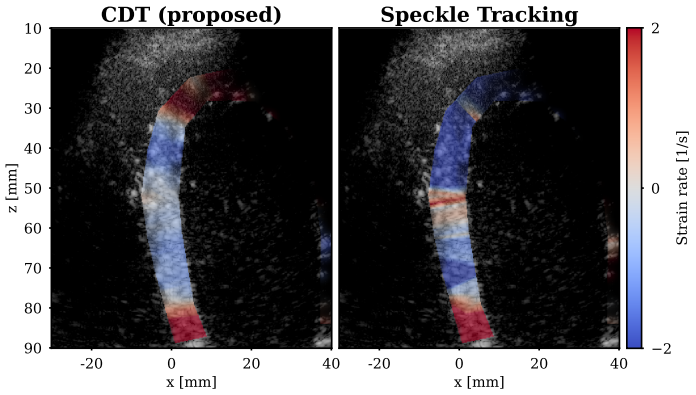

Fig. 4. Strain rate maps recovered from a diverging wave acquisition of a healthy volunteer (apical 4-chamber view). The myocardium was manually delineated and the strain rate maps were computed and are shown in the myocardium.

4 Discussion

We find that CDT is better able to estimate motion vectors from heterogeneous transmit events than block matching when there are clear features to track. In regions with dense speckle we observe larger errors in the estimated motion vectors. This is likely because the modelling assumption of few distinct scatterers is violated in these regions. Another limitation of our method is that the optimization problem is non-convex. This means that large displacements between transmissions can result in a tracking point latching on to a different peak in the next frame, resulting in incorrect motion vectors. In this work we have not

explored the effects of out of plane motion. This is a limitation and should be explored to validate the method in a more realistic setting. Another limitation of our method is its runtime. Solving a set of 3 transmits takes approximately 10-11 seconds on an NVIDIA L40S GPU — several orders of magnitude slower than block matching, which runs in real time. Our implementation is not optimized for speed, and we expect runtime could be reduced through a more efficient implementation and hyperparameter tuning to lower the number of iterations required for convergence. For now, however, the method should be considered offline.

5 Conclusion

We have presented a novel method for estimating strain rate from channel data. We have found increased accuracy over block matching in two simulated phantoms, both in long axis and short axis views. We have also shown that our method is able to recover plausible strain rate maps from in-vivo data. This technique could be a step towards more accurate local strain rate estimation, which would improve the ability to localize ischemic regions in the myocardium and could lead to better treatment outcomes.

Table 1. Mean strain rate error per phantom, location and method.

Phantom	**Location**	**CDT (proposed)**	**Speckle Tracking**
		Error $[1/s] \times 100$	
Ischemic	A (ischemic)	1.4 ± 1.2	5.9 ± 3.8
	B (non-ischemic)	10.6 ± 4.7	18.2 ± 11.4
Ring	A circ.	6.5 ± 5.6	18.6 ± 12.5
	A radial	45.7 ± 29.8	97.7 ± 56.5
	B circ.	17.9 ± 12.1	37.5 ± 21.1
	B radial	13.0 ± 7.6	127.1 ± 38.0
	C circ.	14.0 ± 10.5	30.7 ± 20.1
	C radial	35.8 ± 29.7	141.0 ± 91.5

Acknowledgments. This work was performed within the IMPULSE framework of the Eindhoven MedTech Innovation Center (e/MTIC, incorporating Eindhoven University of Technology and Philips Research), including a PPS supplement from the Dutch Ministry of Economic Affairs and Climate Policy.

Disclosure of Interests. The authors have no competing interests to declare that are relevant to the content of this article.

References

1. Bohs, L., Trahey, G.: A novel method for angle independent ultrasonic imaging of blood flow and tissue motion. IEEE Transactions on Biomedical En-

gineering **38**(3), 280–286 (Mar 1991). https://doi.org/10.1109/10.133210, http://ieeexplore.ieee.org/document/133210/
2. Fraser, A.G., Monaghan, M.J., Van Der Steen, A.F.W., Sutherland, G.R.: A concise history of echocardiography: timeline, pioneers, and landmark publications. European Heart Journal - Cardiovascular Imaging **23**(9), 1130–1143 (Aug 2022). https://doi.org/10.1093/ehjci/jeac111, https://academic.oup.com/ehjcimaging/article/23/9/1130/6619134
3. Ganame, J., Claus, P., Eyskens, B., Uyttebroeck, A., Renard, M., D'hooge, J., Gewillig, M., Bijnens, B., Sutherland, G.R., Mertens, L.: Acute Cardiac Functional and Morphological Changes After Anthracycline Infusions in Children. The American Journal of Cardiology **99**(7), 974–977 (Apr 2007). https://doi.org/10.1016/j.amjcard.2006.10.063, https://linkinghub.elsevier.com/retrieve/pii/S0002914906025021
4. Harkness, A., Ring, L., Augustine, D.X., Oxborough, D., Robinson, S., Sharma, V.: Normal Reference Intervals for Cardiac Dimensions and Function for Use in Echocardiographic Practice: A Guideline from the British Society of Echocardiography. Echo Research & Practice **7**(1), G1–G18 (Mar 2020). https://doi.org/10.1530/ERP-19-0050, https://echo.biomedcentral.com/articles/10.1530/ERP-19-0050
5. Jasaityte, R., Heyde, B., D'hooge, J.: Current State of Three-Dimensional Myocardial Strain Estimation Using Echocardiography. Journal of the American Society of Echocardiography **26**(1), 15–28 (Jan 2013). https://doi.org/10.1016/j.echo.2012.10.005, https://linkinghub.elsevier.com/retrieve/pii/S089473171200795X
6. Kadappu, K.K., Thomas, L.: Tissue Doppler Imaging in Echocardiography: Value and Limitations. Heart, Lung and Circulation **24**(3), 224–233 (Mar 2015). https://doi.org/10.1016/j.hlc.2014.10.003, https://linkinghub.elsevier.com/retrieve/pii/S1443950614007331
7. Kaluzynski, K., Xunchang Chen, Emelianov, S., Skovoroda, A., O'Donnell, M.: Strain rate imaging using two-dimensional speckle tracking. IEEE Transactions on Ultrasonics, Ferroelectrics and Frequency Control **48**(4), 1111–1123 (Jul 2001). https://doi.org/10.1109/58.935730, http://ieeexplore.ieee.org/document/935730/
8. Kerbl, B., Kopanas, G., Leimkuehler, T., Drettakis, G.: 3D Gaussian Splatting for Real-Time Radiance Field Rendering. ACM Transactions on Graphics **42**(4), 1–14 (Aug 2023). https://doi.org/10.1145/3592433, https://dl.acm.org/doi/10.1145/3592433
9. Kingma, D.P., Ba, J.: Adam: A Method for Stochastic Optimization. In: 3rd International Conference on Learning Representations (ICLR 2015). arXiv, San Diego, CA, USA (2015). https://doi.org/10.48550/ARXIV.1412.6980, https://arxiv.org/abs/1412.6980, version Number: 9
10. Leclerc, S., Smistad, E., Pedrosa, J., Ostvik, A., Cervenansky, F., Espinosa, F., Espeland, T., Berg, E.A.R., Jodoin, P.M., Grenier, T., Lartizien, C., Dhooge, J., Lovstakken, L., Bernard, O.: Deep Learning for Segmentation Using an Open Large-Scale Dataset in 2D Echocardiography. IEEE Transactions on Medical Imaging **38**(9), 2198–2210 (Sep 2019). https://doi.org/10.1109/TMI.2019.2900516, https://ieeexplore.ieee.org/document/8649738/
11. Lorenz, C., Pastorek, J., Bundy, J.: Function: Delineation of Normal Human Left Ventricular Twist Throughout Systole by Tagged Cine Magnetic Resonance Imaging. Journal of Cardiovascular Magnetic Resonance

2(2), 97–108 (May 2000). https://doi.org/10.3109/10976640009148678, http://www.informaworld.com/openurl?genre=article&doi=10.3109/10976640009148678&magic=crossref||D404A21C5BB053405B1A640AFFD44AE3
12. Matrone, G., Savoia, A.S., Caliano, G., Magenes, G.: The Delay Multiply and Sum Beamforming Algorithm in Ultrasound B-Mode Medical Imaging. IEEE Transactions on Medical Imaging **34**(4), 940–949 (Apr 2015). https://doi.org/10.1109/TMI.2014.2371235, https://ieeexplore.ieee.org/document/6960091, conference Name: IEEE Transactions on Medical Imaging
13. Selfridge, A.R., Kino, G.S., Khuri-Yakub, B.T.: A theory for the radiation pattern of a narrow-strip acoustic transducer. Applied Physics Letters **37**(1), 35–36 (Jul 1980). https://doi.org/10.1063/1.91692, https://pubs.aip.org/apl/article/37/1/35/526883/A-theory-for-the-radiation-pattern-of-a-narrow
14. Stevens, T.S.W., van Nierop, W.L., Luijten, B., van de Schaft, V., Nolan, O., Federici, B., Penninga, S.W., Schueler, N.I., van Sloun, R.J.G.: Zea: A Toolbox for Cognitive Ultrasound Imaging (2025), https://github.com/tue-bmd/zea, tex.eprint: 2512.01433
15. Trahey, G.E., Allison, J.W., Von Ramm, O.T.: Angle Independent Ultrasonic Detection of Blood Flow. IEEE Transactions on Biomedical Engineering **BME-34**(12), 965–967 (Dec 1987). https://doi.org/10.1109/TBME.1987.325938, http://ieeexplore.ieee.org/document/4122484/
16. Van De Schaft, V., Nolan, O., Van Sloun, R.J.G.: Off-Grid Ultrasound Imaging by Stochastic Optimization. IEEE Transactions on Ultrasonics, Ferroelectrics, and Frequency Control **72**(9), 1245–1255 (Sep 2025). https://doi.org/10.1109/TUFFC.2025.3586377, https://ieeexplore.ieee.org/document/11073078/
17. Weidemann, F., Wacker, C., Rauch, A., Bauer, W.R., Bijnens, B., Sutherland, G.R., Ertl, G., Voelker, W., Fidler, F., Strotmann, J.M.: Sequential Changes of Myocardial Function During Acute Myocardial Infarction, in the Early and Chronic Phase After Coronary Intervention Described by Ultrasonic Strain Rate Imaging. Journal of the American Society of Echocardiography **19**(7), 839–847 (Jul 2006). https://doi.org/10.1016/j.echo.2006.01.024, https://linkinghub.elsevier.com/retrieve/pii/S0894731706001842
18. zeahub: zea-cardiac-2026. Hugging Face Datasets (2026), https://huggingface.co/datasets/zeahub/zea-cardiac-2026, accessed 2026-07-08
19. Zhao, Y., Pang, G., Sun, Z., Liu, Y., Lv, L., Li, T., Jiang, T., Li, Z., Xu, J., Xing, J., Babyn, P., Yao, G., Sun, F.r.: Block Matching Based Speckle Tracking Echocardiography: Clinical Applications and Research Outlook in a Deep Learning Context. Journal of Imaging Informatics in Medicine (Dec 2025). https://doi.org/10.1007/s10278-025-01750-w, https://link.springer.com/10.1007/s10278-025-01750-w